NANO · MICRO small
www.small-journal.com

Unravelling H^+/Zn^{2+} Synergistic Intercalation in a Novel Phase of Manganese Oxide for High-Performance Aqueous Rechargeable Battery

*Qinghe Zhao, Xin Chen, Ziqi Wang, Luyi Yang, Runzhi Qin, Jinlong Yang, Yongli Song, Shouxiang Ding, Mouyi Weng, Weiyuan Huang, Jiajie Liu, Wenguang Zhao, Guoyu Qian, Kai Yang, Yanhui Cui, Haibiao Chen, and Feng Pan**

Aqueous Zn-MnO_2 batteries using mild electrolyte show great potential in large-scale energy storage (LSES) application, due to high safety and low cost. However, structure collapse of manganese oxides upon cycling caused by the conversion mechanism (e.g., from tunnel to layer structures for α-, β-, and γ-phases) is one of the most urgent issues plaguing its practical applications. Herein, to avoid the phase conversion issue and enhance battery performance, a structurally robust novel phase of manganese oxide $MnO_2H_{0.16}(H_2O)_{0.27}$ (MON) nanosheet with thickness of ≈2.5 nm is designed and synthesized as a promising cathode material, in which a nanosheet structure combined with a novel H^+/Zn^{2+} synergistic intercalation mechanism is demonstrated and evidenced. Accordingly, a high-performance Zn/MON cell is achieved, showing a high energy density of ≈228.5 Wh kg^{-1}, impressive cyclability with capacity retention of 96% at 0.5 C after 300 cycles, as well as exhibiting rate performance of 115.1 mAh g^{-1} at current rate of 10 C. To the best current knowledge, this H^+/Zn^{2+} synergistic intercalation mechanism is first reported in an aqueous battery system, which opens a new opportunity for development of high-performance aqueous Zn ion batteries for LSES.

Rechargeable aqueous Zn-based batteries are attractive for large-scale energy storage (LSES), due to their low cost, high safety, and eco-friendliness, as well as high ionic conductivity of the aqueous electrolyte.[1,2] Among the most studied cathode materials, such as Prussian blue analogues[3,4] and vanadium-based oxides,[5,6] manganese oxides are more promising for practical use of aqueous Zn ion batteries, attributing to both the high operating cell voltage and considerable capacity delivery.[7,8] However, the structure collapse of MnO_2 (α-, β-, γ-, etc.) upon cycling, due to a combined effect of Mn^{2+} dissolution,[8] phase conversion,[9,10] collapse of layered structure,[11,12] and formation of inactive by-products,[13,14] usually results in rapid capacity fading and then its practical application is restricted.

Reaction mechanism of MnO_2 in neutral or mild acid electrolytes remains controversial. Different reaction mechanisms, intercalation or conversion, have been reported for MnO_2 with various crystal structures (α-, β-, γ-, δ-, λ-, δ-, or amorphous). MnO_2 with tunnel structures, such as α-,[10] β- ,[15] and γ-MnO_2,[16] usually show a conversion mechanism, in which a tunnel structure of MnO_2 can transform into a layered structure upon H^+ and/or Zn^{2+} insertion. After long-term cycle, some inactive by-products (e.g., woodruffite $ZnMn_3O_7$[13]) with low electrochemical activity will form, leading to a serious capacity fading. A single Zn^{2+} intercalation mechanism has been revealed for layered δ-MnO_2,[11,17] spinel-type $ZnMn_2O_4$,[18,19] and Mn_3O_4,[20,21] and despite of excellent cyclability, their reversible capacity is much lower than that of the α-, β-, and γ- MnO_2. The amorphous MnO_2[22,23] obtained from electrodeposition shows an impressive electrochemistry, however, it is not clear whether it follows intercalation or conversion mechanism during discharge. Moreover, its practical use is restricted by the low loading of active material. Meanwhile, compared with Zn^{2+}, the monovalent H^+ with smaller ion radius shows high ion diffusion kinetics, and thus the utilization of H^+ insertion is vital to improve the rate performance of Zn-MnO_2 battery.[24,25] By tuning nanostructure of MnO_2 cathode, H^+ and Zn^{2+} synergistic intercalation mechanism can be obtained, which is the key to improve the electrochemical performance of Zn-MnO_2 battery, including capacity, cycling stability, and rate capability.

Herein, a novel phase of manganese oxide nanosheet (MON, thickness of ≈2.5 nm) was synthesized as a cathode for aqueous Zn battery (**Figure 1**a). The 1 × 1 tunnels of MON act as structurally robust hosts for the H^+/Zn^{2+} synergistic intercalation/extraction upon cycling. A H^+/Zn^{2+} synergistic intercalation mechanism is obtained and evidenced, and MON cathode presents an excellent cycling stability (capacity retention of 96% at 0.5 C after 300 cycles), compared with β-MnO_2 based on a conversion mechanism (Figure 1b; Figure S1, Supporting

Dr. Q. Zhao, X. Chen, Dr. Z. Wang, Dr. L. Yang, Dr. R. Qin, Dr. J. Yang, Dr. Y. Song, S. Ding, Dr. M. Weng, W. Huang, J. Liu, W. Zhao, Dr. G. Qian, K. Yang, Dr. Y. Cui, Prof. H. Chen, Prof. F. Pan
School of Advanced Materials
Peking University Shenzhen Graduate School
Shenzhen 518055, P. R. China
E-mail: panfeng@pkusz.edu.cn

The ORCID identification number(s) for the author(s) of this article can be found under https://doi.org/10.1002/smll.201904545.

DOI: 10.1002/smll.201904545

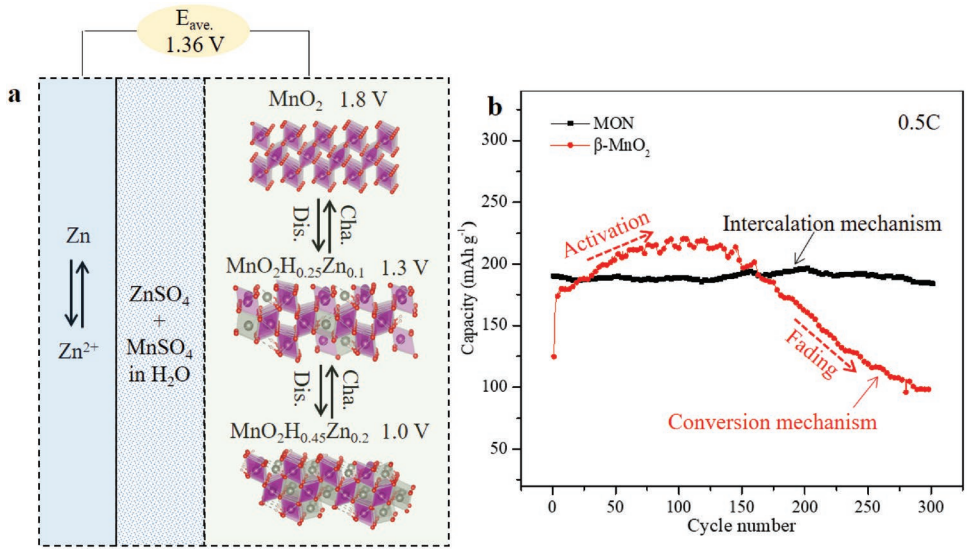

Figure 1. Zn/MON battery chemistry. a) Schematic illustration of the rechargeable aqueous Zn/MON cell using 1 M $ZnSO_4$ + 0.2 M $MnSO_4$ electrolyte. b) Comparison of the cycling performance of Zn/MON and Zn/β-MnO_2 cells at current density of 0.5 C (1 C = 308 mAh g^{-1}).

Information). The Zn/MON battery also shows high energy density as well as superior rate performance. Based on the superior battery performance, the proposed Zn/MON battery is a promising system for LSES.

The MON was prepared by a simple one-step hydrothermal reaction process (Figure S2, Supporting Information). The crystal structure of MON is characterized by X-ray diffraction (XRD) (**Figure 2**a), indicating good crystallinity of MON. All peaks are indexed to a monoclinic crystal phase of manganite (PDF # 41-1379), and no other peaks of impurities can be detected. The new phase of manganite belongs to the $P2_1/c$ (14) space group with 1 × 1 tunnel structure. Scanning electron

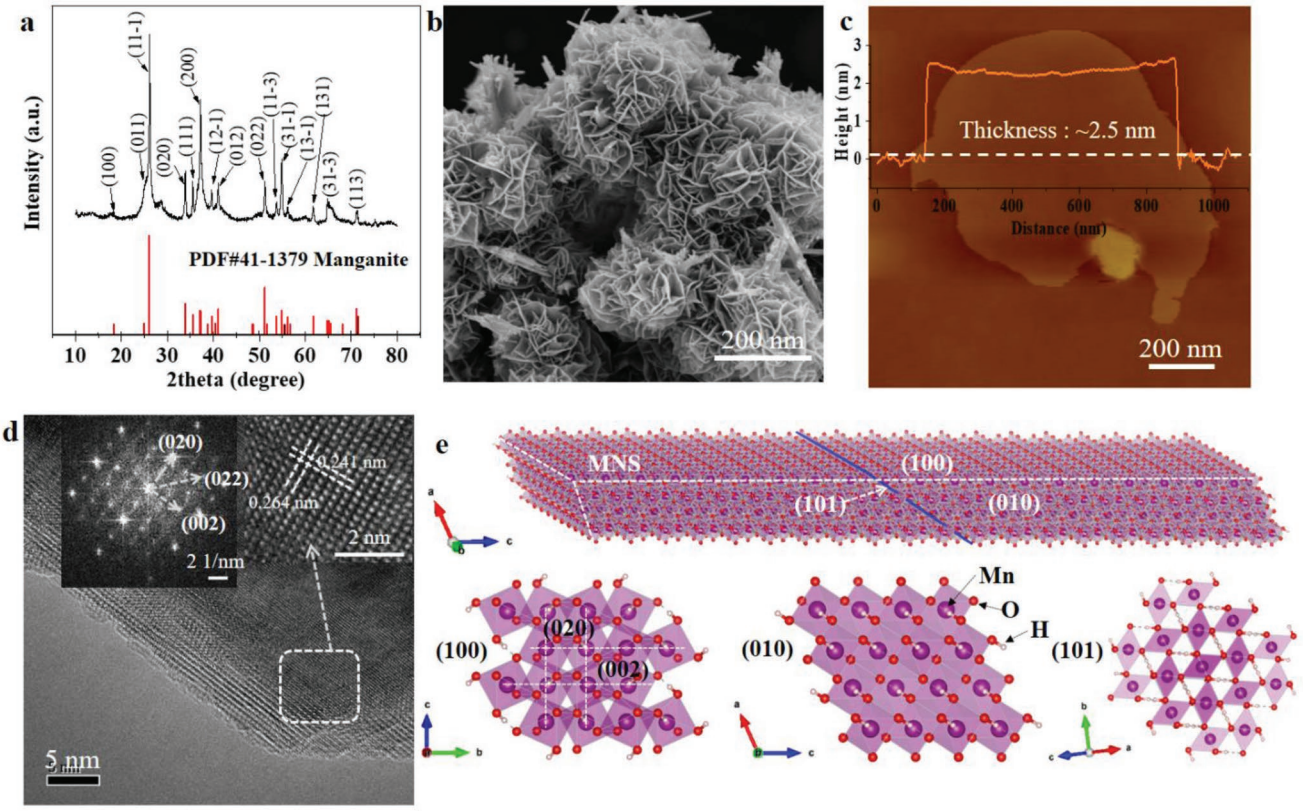

Figure 2. Material characterization of the as-prepared MON material. a) XRD pattern, b) SEM morphology, c) AFM image; d) TEM image, and e) schematic illustration of polyhedral models of MON. Inset in (d) shows HR-TEM image and diffraction pattern of (100) plane.

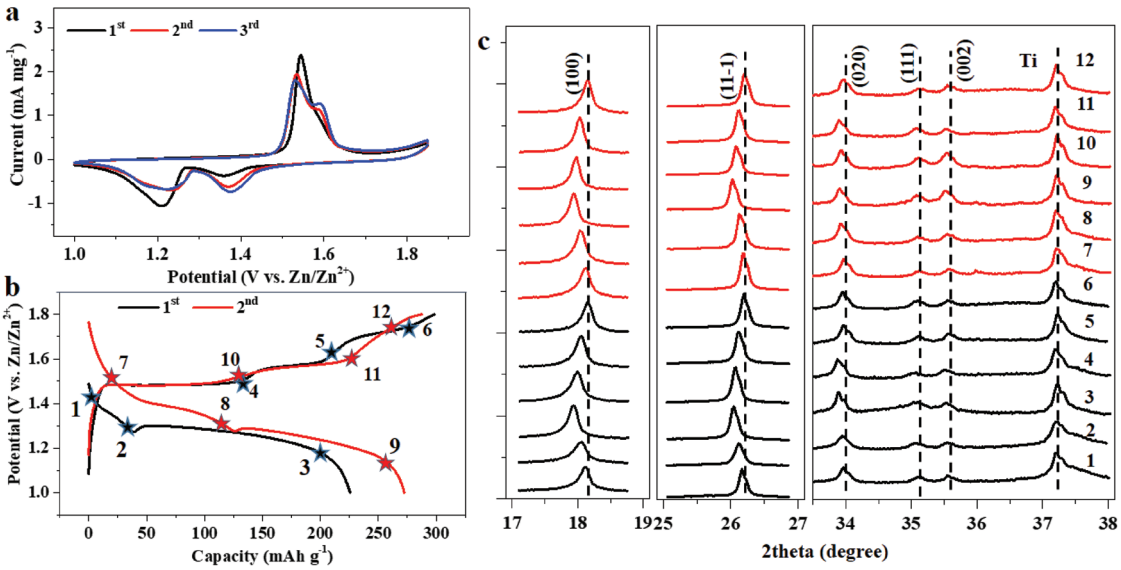

Figure 3. Electrochemical and structural evolution of MON in Zn/MON cell. a) Cyclic voltammograms of MON electrode at a scan rate of 0.2 mV s^{-1} from 0.95 to 1.85 V. b) Typical charge/discharge curves for the initial two cycles at 0.1 C in 1 M $ZnSO_4$ + 0.2 M $MnSO_4$ aqueous electrolyte. c) XRD patterns of MON electrode at selected states from point 1 to 12 in (b) during the 1st and 2nd cycles. The electrodes are immersed in a distilled acetic acid to remove the $Zn_4SO_4(OH)_6(H_2O)_5$ on electrode surface before XRD tests.

microscopy (SEM) image of MON shows a hierarchical structure with nanosheets arranging perpendicularly from the core, with a diameter of ≈300 nm (Figure 2b). The nanocrystal and mesoporous feature of MON can provide abundant electrochemical interfaces and reduces the ion diffusion distance, enabling fast electrochemical kinetics, which is further supported by an obvious hysteresis loop in the nitrogen adsorption–desorption isotherms, along with a surface area of ≈120 m^2 g^{-1} and a pore size centered at ≈3.5 nm (Figure S3, Supporting Information). To measure the thickness of the nanosheet, atomic force microscopy (AFM) was conducted. The average thickness of as-prepared MON measured from height profile of AFM image (Figure 2c; Figure S4, Supporting Information) is ≈2.5 nm. The chemical formula of MON was also demonstrated as $MnO_2H_{0.16}(H_2O)_{0.27}$, based on a combined analysis from XPS results (Figure S5, Supporting Information), thermogravimetric analysis results (Figure S6, Supporting Information), and an inverse titration measurement (Inverse titration measurement section in the Supporting Information).

The nanocrystal structure of MON is further investigated by high-resolution transmission electron microscopy (HR-TEM) (Figure 2d), which shows a well-resolved lattice fringes, with lattice spacing of 0.264 and 0.241 nm, corresponding to the d_{002} and d_{020} interlayer spacing, respectively, and the diffraction pattern from fast Fourier transform (FFT) images is also consistent with that of HR-TEM results. Based on the XRD and HR-TEM results, the 1 × 1 tunneled nanostructure of MON is shown in Figure 2e. It can be seen that the (100) plane of MON is the exposed surface, and (020) and (002) interlayers with angle value of 90° are presented on the exposed (100) plane surface as shown in the HR-TEM result (Figure 1d). For MON, MnO_6 octahedras are assembled into edge-sharing chains, which then form a 1 × 1 tunneled framework structure by connecting corners. The 1 × 1 tunnels on the crystallographic (101) plane of MON act as H^+ and Zn^{2+} insertion/extraction channels, which will be discussed in detail later. The nanostructure of β-MnO_2 is shown in Figure S7 in the Supporting Information. Compared with β-MnO_2, MON presents an obviously larger exposed area for 1 × 1 tunnels, which results in different reaction mechanisms and battery performance of MON and β-MnO_2.

Figure 3a shows the cyclic voltammograms (CVs) of MON in aqueous 1 M $ZnSO_4$ + 0.2 M $MnSO_4$ electrolyte, from which two peaks at 1.361 and 1.211 V versus Zn/Zn^{2+} are observed during the 1st cathodic sweeping. In the following two cycles, the CV curves with nearly overlapped two cathodic peaks located at 1.375 and 1.231 V are observed. The difference in CV profiles between the 1st and subsequent two cycles is mainly due to the activation process. Additionally, both CV profiles for the 1st and subsequent two cycles present similar two discharge peaks, which is much different from that of β-MnO_2 (Figure S8, Supporting Information), suggesting an intercalation mechanism for MON cathode. Figure 3b shows the galvanostatic charge/discharge curves of MON at 0.1 C, and both the 1st and 2nd discharge curves present two discharge plateaus, in line with the CV results in Figure 3a. Notably, the reversible discharge capacity in 2nd cycle reaches ≈275 mAh g^{-1}, which is one of the highest utilization reported with nearly ≈90% of the theoretical capacity of MnO_2 (≈308 mAh g^{-1} for 1 e^- transfer of MnO_2, Table S1, Supporting Information).

To investigate the structural evolution of MON during the discharge/charge process, ex situ XRD patterns (Figure S9, Supporting Information) were obtained at the selected states from points 1 to 12 (marked in Figure 3b). Large amount of $Zn_4SO_4(OH)_6(H_2O)_5$ (PDF#39-0688) is observed for discharged electrodes at points of 2, 3, 8, and 9, suggesting a H^+ intercalation upon discharge, which is consistent with the previously reported results.[26] The formation of $Zn_4SO_4(OH)_6(H_2O)_5$ is also evidenced by SEM and TEM results (Figures S10 and S11,

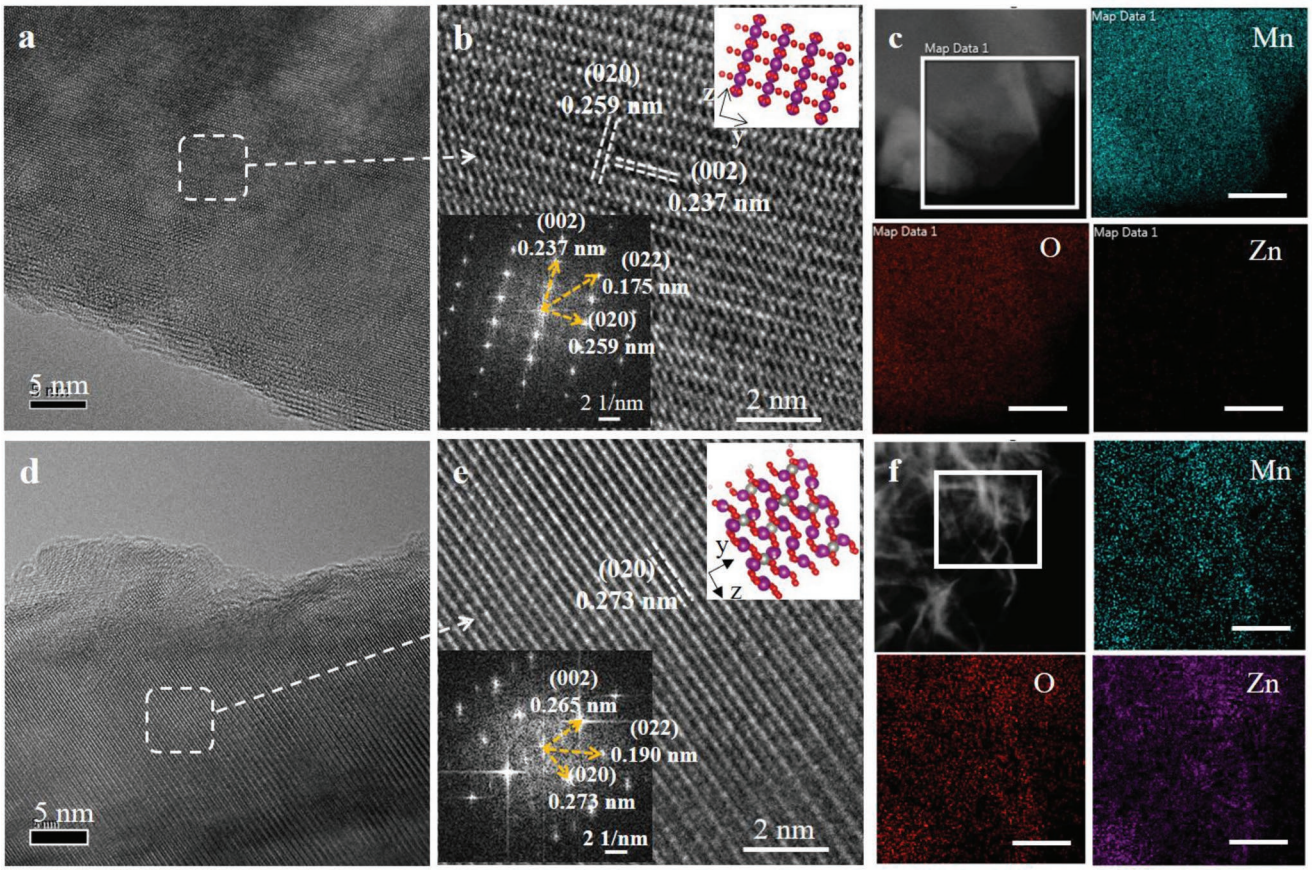

Figure 4. Microstructural and compositional analysis of the discharged MON cathode at point 7 and 9 in Figure 3b. TEM and HRTEM images of MON at a) point 7 and d) 9. HRTEM and FFT images of MON at b) point 7 and e) 9. STEM–EDS mappings for elements of Mn, Zn, and S for MON electrodes at (c) point 7 and f) 9.

Supporting Information). Besides, to make the structural evolution of MON more clear, all electrodes are immersed in a distilled acetic acid to remove the $Zn_4SO_4(OH)_6(H_2O)_5$ on electrode surface, and the obtained XRD patterns are shown in Figure 3c. Only the characteristic peaks of MON can be observed, which is obviously different from that of previously reported species (e.g., spinel $ZnMn_2O_4$,[12] MnOOH,[25] and tunneled γ-Zn_xMnO_2,[16] and Zn-buserite phase[9]). The peaks of (100) and (11-1) planes of MON show obvious shift toward smaller angles upon discharging, and then shift back upon charging, indicating a reversible lattice expansion and contraction process. Thus, an intercalation mechanism is confirmed for MON, which is beneficial to its cyclability. We also investigated the phase evolution of β-MnO_2 (Figure S1, Supporting Information), where a phase transition from β-MnO_2 to spinel-type $ZnMn_2O_4$ during discharge as well as the accumulation of $ZnMn_2O_4$ can be observed (Figure S12, Supporting Information), suggesting a conversion mechanism, which contributes to the capacity fading of β-MnO_2 cathode after long-term cycle.

The structural evolution of MON cathode is further investigated by TEM analysis. **Figure 4**a,b gives the HRTEM and corresponding FFT images at the discharge state of point 7 in Figure 3b, where the lattice fringes can be indexed to (020) and (002) planes. TEM elemental mapping in Figure 4c shows that the Zn concentration in MON is barely visible, indicating that only H^+ intercalation occurs in initial discharge state of MON in the 1st discharge plateau. The microstructure of fully discharged MON (point 9) cathode is shown in Figure 4d,e, where an obvious lattice expansion of (020) and (002) planes is observed compared with MON at point 7, and a significant amount of Zn^{2+} concentration is observed in MON (Figure 4f). Thus, according to the above XRD and TEM results, both the H^+ and Zn^{2+} intercalations contribute to the discharge capacity of Zn/MON cell.

To clarify the H^+ and Zn^{2+} synergistic intercalation mechanism, further investigation is performed. **Figure 5**a shows the discharge curves of MON in different electrolytes. When discharged to 0.4 V, for MON cathode, a single H^+ intercalation in $MnSO_4$ aqueous electrolyte contributes a capacity of ≈167 mAh g^{-1}, and a single Zn^{2+} intercalation in $ZnSO_4$ nonaqueous dimethyl sulfoxide (DMSO) electrolyte demonstrates a capacity of ≈154 mAh g^{-1}, however, both the single H^+ and Zn^{2+} intercalations show lower discharge capacity than that of the H^+ and Zn^{2+} synergistic intercalation (≈305 mAh g^{-1}, $ZnSO_4$ + $MnSO_4$ aqueous electrolyte). X-ray photoelectron spectroscopy (XPS) analyses (Figure 5b,c) are further used to characterize the H^+ and Zn^{2+} synergistic intercalation mechanism. For Mn 3s spectra in Figure 5b, when the discharge depth increases, a new Zn 3p peak raises and enhances gradually at binding energy of ≈91.4 eV, indicating a successful Zn^{2+} intercalation during both the 1st and 2nd discharge plateaus. In

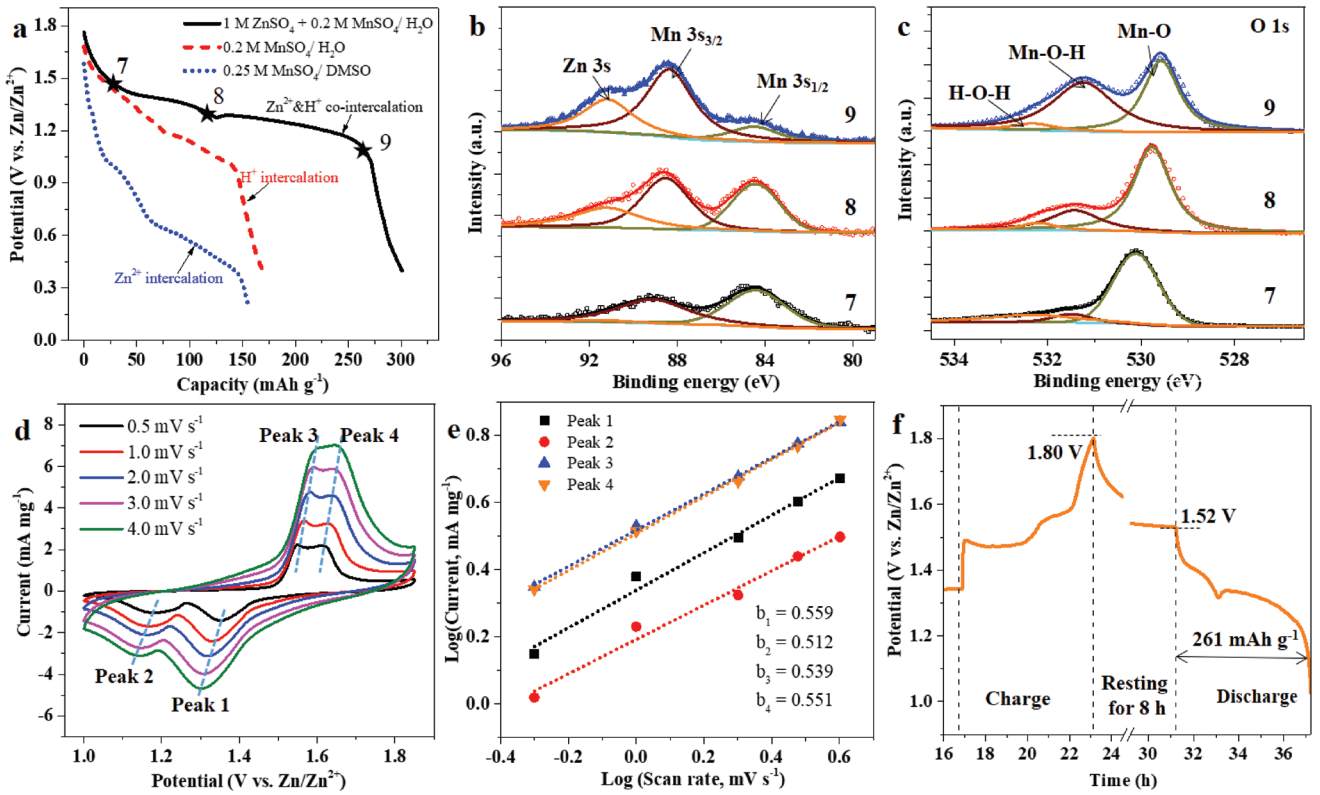

Figure 5. Zn^{2+} and H^+ cointercalation mechanism. a) The discharge profile of MON cathode at current of 0.1 C in different electrolytes (black: 1 M $ZnSO_4$ + 0.2 M $MnSO_4$ in H_2O; red: 0.2 M $MnSO_4$ in H_2O; blue: 0.25 M $MnSO_4$ in DMSO). b,c) XPS spectrums of MON electrodes at discharge states from points 7 to 9 in Figure 3b. d) CV curves of Zn/MON cells at different scan rates. e) b-value of redox peaks from 1 to 4, according to $i = a \cdot v^b$ (i is current, v is scan rate, a and b are variable values), and b_n value indicates the b value of peak n in the CV curves in (a). f) Self-discharge test by resting for 8 h at fully charged state.

Figure 5c, the intensity of Mn–O–H peak increases gradually with increasing discharge depth, confirming the presence of H^+ in the tunnels of MON after discharge process. Besides, the reduced Mn valence of MON after H^+ and Zn^{2+} intercalation is also demonstrated (Figure S13, Supporting Information).

The charging/discharging kinetic parameters of MON cathode (solid diffusion or capacitive adsorption of H^+ and Zn^{2+}) is identified by analyzing the redox reactions presented in the CV curves at different scan rates (Figure 5d,e). CV curves are conducted in 1 M $ZnSO_4$ and 0.2 M $MnSO_4$ electrolyte, and the addition of $MnSO_4$ is used to suppress the Mn^{2+} dissolution from MON during discharge. Two pairs of redox peaks denoted as peak 1, 2, 3, and 4 are observed (Figure 5d), indicating two charge/discharge redox reactions. The charge storage kinetics are identified by the relationship between the current value of peaks (i) and the scanning rates (v): $i = a \cdot v^b$, where a and b are variable values.[27–29] The value of b is in a range of 0.5 to 1: when $b = 0.5$, the solid diffusion of H^+/Zn^{2+} dictates the charge/discharge process; when $b = 1$, the surface electrochemical capacitive adsorption of H^+/Zn^{2+} is predominant. The dependence curves and corresponding fitting curves between log (i) and log (v) for the four redox peaks are plotted in Figure 5e. The result indicates that the fitted b value of all peaks are approaching 0.5 (0.559, 0.512, 0.539, and 0.551 for redox peaks 1 to 4, respectively), indicating a solid diffusion controlled kinetic of MON during charge/discharge process. The detailed separation of diffusion-type and capacitive-type capacities is shown in Figure S14 in the Supporting Information, which also confirms the diffusion-controlled kinetic of MON cathode. The self-discharge curve of MON is also conducted to identify the H^+ and Zn^{2+} diffusion controlled kinetics of MON by resting for 8 h after fully charged to 1.8 V. As a result, Figure 5f shows a high capacity retention of 95.1% comparing with the original discharge capacity (275 mAh g^{-1}), and demonstrates the solid diffusion dominated kinetics of MON.

To further clarify the H^+ and Zn^{2+} contributions to capacity delivery of MON, a quantitative chemical analysis is carried out using a inductively coupled plasma mass spectrometry (ICP-MS), as shown in **Figure 6**a. By analyzing the ICP-MS results, the quantitative H^+ and Zn^{2+} intercalation during discharge is revealed. For the 1st discharge plateau (1.8–1.3 V), about 0.255 mol H^+ and 0.086 mol Zn^{2+} are intercalated into 1 mol MON, and during the 2nd discharge plateau (1.3–1.0 V), another 0.204 mol H^+ and 0.142 mol Zn^{2+} are intercalated. Thus, based on the ICP-MS results, the electrochemical reaction of the Zn/MON battery can be formulated as below

Cathode reaction

$$MnO_2 + 0.45\,H_2O + 0.225\,Zn^{2+} + 0.9\,e^- \rightarrow MnO_2H_{0.45}Zn_{0.225} + 0.45\,OH^- \quad (1)$$

$$0.3\,ZnSO_4 + 0.45\,OH^- \rightarrow 0.075\,Zn_4(OH)_6SO_4 + 0.225\,SO_4^{2-} \quad (2)$$

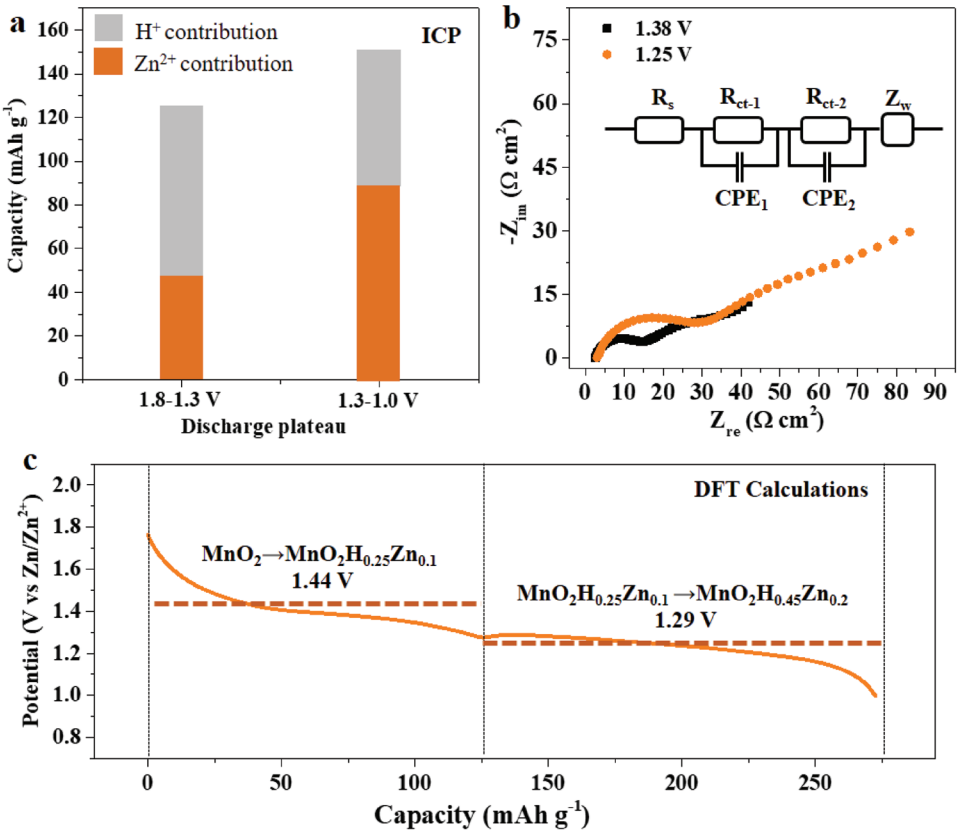

Figure 6. Quantitative analysis of electrochemical reaction of Zn/MON cell. a) Quantitative Zn^{2+} and H^+ contribution to capacity delivery according to ICP results. b) EIS analysis of Zn/MON cells at discharged state of 1.38 and 1.25 V in the 1st and 2nd discharge plateaus. c) Illustration of voltage of Zn/MON cells from DFT calculations for the 1st and 2nd discharge plateaus.

Anode reaction

$$0.45\,Zn \rightarrow 0.45\,Zn^{2+} + 0.9\,e^- \quad (3)$$

Overall

$$MnO_2 + 0.45H_2O + 0.075ZnSO_4 + 0.45Zn \leftrightarrow MnO_2Zn_{0.225}H_{0.45} + 0.075Zn_2(OH)_6SO_4 \quad (4)$$

Taking the total mass of reactants in Equation (4) into consideration, the Zn/MON battery provides an impressive energy density of ≈228.5 Wh kg^{-1} (at 0.1 C), which is about six times higher than that of the commercialized lead-acid battery, presenting huge promise in LSES field. Electrochemical impedance spectroscopy (EIS) spectra are also tested and plotted to demonstrate the H^+/Zn^{2+} intercalation behavior at potential of 1.38 (in 1st discharge plateau) and 1.25 V (in 2nd discharge plateau), respectively (Figure 6b). Both EIS plots show two Ohm capacitive resistances and a diffusion tail, representing H^+ and Zn^{2+} intercalation and diffusion process. Besides, the resistance in 2nd discharge plateau is higher than that in the 1st plateau, indicating a gradually slowed diffusion kinetics of H^+ and Zn^{2+} as discharge depth increases. The galvanostatic intermittent titration technique (GITT, Figure S15, Supporting Information) result also shows a larger overpotential in the 2nd discharge plateau compared with that in the 1st discharge plateau, in line with the EIS results.

The H^+ and Zn^{2+} synergistic intercalation mechanism of MON is also demonstrated by calculating the thermodynamics of discharged MON using density functional theory (DFT) method. In this work, for MON cathode, ≈0.255 mol H^+ and ≈0.086 mol Zn^{2+} are intercalated into 1 mol MON in the 1st discharge plateau, and another ≈0.204 mol H^+ and ≈0.142 mol Zn^{2+} are intercalated in the 2nd discharge plateau. To simplify the calculation, voltage of the 1st discharge plateau is determined by potential difference between $MnO_2/MnO_2H_{0.25}Zn_{0.1}$ and Zn/Zn^{2+} redox reactions, while for the 2nd discharge plateau, the cell voltage is attributed to the potential difference between $MnO_2H_{0.25}Zn_{0.1}/MnO_2H_{0.45}Zn_{0.2}$ and Zn/Zn^{2+} redox reactions. Detailed calculation processes and results are demonstrated in Figures S16, S17, and DFT calculations section in the Supporting Information. An average cell voltage value of 1.44 and 1.29 V are obtained for the 1st and 2nd discharge plateaus, respectively (Figure 5c), which is consistent with the experimental discharge profiles, and demonstrates the veracity of H^+/Zn^{2+} synergistic intercalation mechanism.

The electrochemical performance of Zn/MON rechargeable battery is characterized by a typical 2032 coin-type cell consisting of a MON cathode (active loading ≈ 2.5 mg cm^{-2}), zinc metal anode, and a home-made mesoporous Silica-PTFE

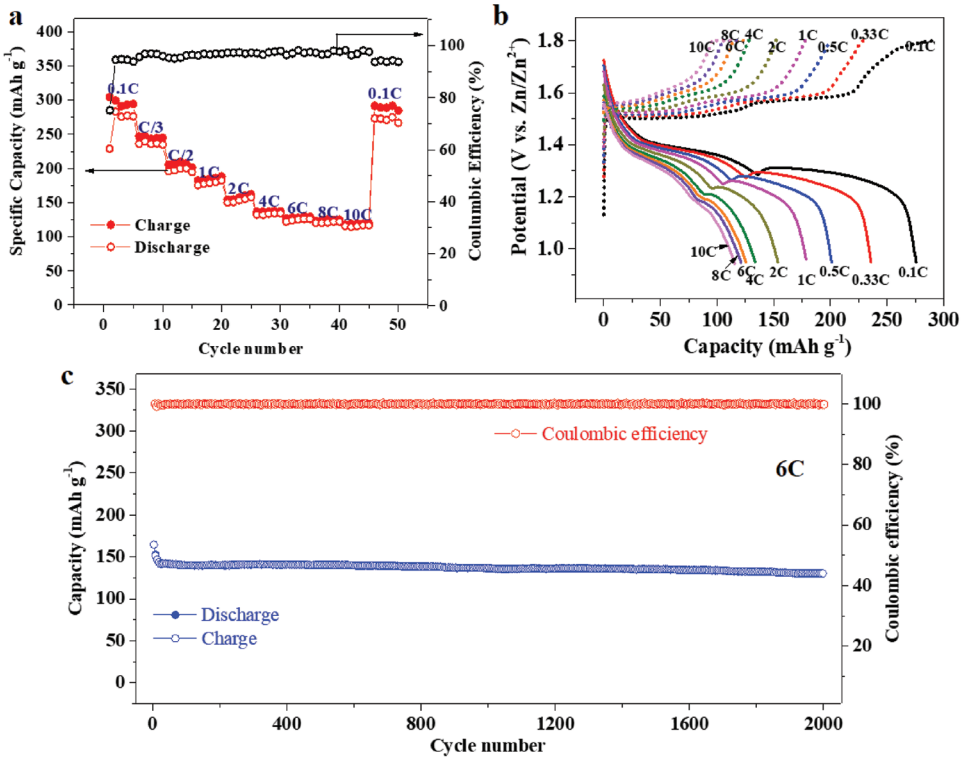

Figure 7. Battery performance of the Zn/MON cell. a,b) Rate performance and charge/discharge profiles of the cell at current densities varying from 0.1 C to 10 C (1 C = 308 mA g^{-1}). c) Cycling performance in terms of specific capacity (blue) and the corresponding Coulombic efficiency (red) at a current density of 6 C.

(MS-PTFE) separator absorbed with aqueous electrolyte (1 M $ZnSO_4$ + 0.2 M $MnSO_4$) (Figures S18 and S19, Supporting Information). The home-made MS-PTFE separator is tough enough to depress the zinc dendrite growth, and thus guarantees a long-term cycle test for a Zn/MON battery. **Figure 7**a,b presents the rate performance of Zn/MON cell from current of 0.1 C to 10 C. Discharge capacities of 275.6, 235.8, 201.1, 178.6, 153.6, 133.5, 125.7, 121.2, and 115.1 mAh g^{-1} are recorded at 0.1 C, 0.33 C, 0.5 C, 1 C, 2 C, 4 C, 6 C, 8 C, and 10 C, respectively. The superior discharge capacity of 115.1 mAh g^{-1} at 10 C, with a middle discharge voltage of 1.36 V, can be hardly achieved by other MnO_2 analogue cathodes (Table S2, Supporting Information). In addition, after cycling back to 0.1 C, an average discharge capacity of 273.3 mAh g^{-1} can be well recovered, which is equivalent to 99.2% of the initial average capacity (275.6 mAh g^{-1}), showing an excellent structure stability of MON cathode against H^+ and Zn^{2+} intercalation/extraction. Besides, with the increasing discharge rate, the voltage and capacity drops in both the 1st and 2nd discharge plateaus, which is different from the result from Wang's group[24] (with increasing current rate, capacity and voltage remains unchanged in the 1st discharge plateau, while drops obvious in the 2nd discharge plateau for a electrodeposited MnO_2), demonstrating a H^+/Zn^{2+} synergistic intercalation in both the 1st and 2nd discharge plateaus. The superior rate property of MON can be further demonstrated by XPS results in **Figure 8**a,b, which show that H^+ intercalation dominates the discharge capacity of MON at high rate of 10 C, rather than Zn^{2+} intercalation. The diffusion kinetic of H^+ is much higher than that of Zn^{2+}, due to the relative smaller ion radius and lower electrostatic interaction,[30] thus the H^+ intercalation benefits a lot to the high rate performance of MON.

To evaluate the cyclability of MON cathode, Zn/MON battery was also galvanostatically cycled for 300 cycles at 0.5 C (Figure 1b), and 2000 cycles at 6 C (Figure 7c). When cycled at 0.5 C, the reversible capacity sustains 197 mAh g^{-1} with a capacity retention of 96.4% after 300 cycles. Reversible capacity at 6 C rate starts from 163.5 mAh g^{-1}, decreases quickly to 148.5 mAh g^{-1} in 10 cycles, and then decreases slowly to 131.6 mAh g^{-1} within 2000 cycles, with a capacity retention of 79.0% and a Coulombic efficiency approaching 100%, which is an excellent cyclability for a manganese oxide cathode in aqueous Zn battery (Table S3, Supporting Information). The superior cyclability of MON is mainly attributed to its robust structure against the H^+ and Zn^{2+} intercalation/extraction, as evidenced in Figure 8c, which shows only the pure MON phase for fully charged MON cathodes after 5–300 cycles at rate of 0.5 C. TEM results in Figure S20 in the Supporting Information also shows a well maintained crystalline structure of MON cathode after 100 cycles at 0.5 C, demonstrating a high structure stability upon cycling, which is vital for the superior cyclability for MON. Besides, all CV curves (0.5 mV s^{-1}) within 300 cycles at 0.5 C present two clear discharge peaks representing two discharge processes (Figure 8d), which also demonstrates the high cycling stability of MON cathode.

From the above results, a high-performance aqueous Zn/MON cell with a superior capacity, rate, and cycling

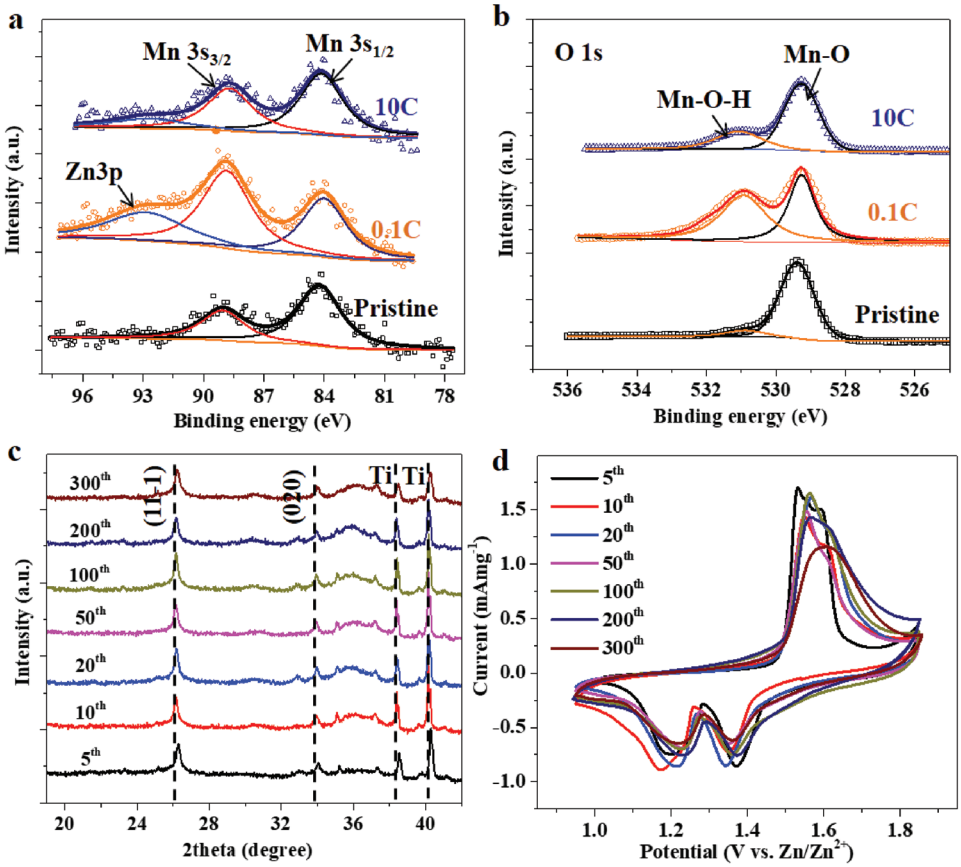

Figure 8. a,b) XPS analyses of Mn3s and O1s spectrums for MON cathode at pristine, discharged at 0.1 C and 10 C. c) XRD patterns of MON electrodes and d) CV curves of Zn/MON cells after different cycles at 0.5 C.

performance is presented, and a novel H^+/Zn^{2+} synergistic intercalation mechanism during discharge is also demonstrated. The H^+/Zn^{2+} cointercalation is vital for the high capacity of MON (275.6 mAh g^{-1} at 0.1 C) since under a single-ion intercalation mechanism, the capacity release shall reduce obviously.[31–33] Besides, the intercalation of H^+ and Zn^{2+} promotes each other thermodynamically. The excellent cyclability of MON cathode is summarized as follow: first, the H^+/Zn^{2+} intercalation/extraction is highly reversible in the MON with tough structural stability; second, a novel nanostructure of MON (≈2.5 nm) with large amount of exposed 1 × 1 tunnels as channels for H^+ and Zn^{2+} intercalation/extraction benefits a lot on the cycling performance. The obtained rate performance of MON cathode is mainly attributed to H^+ intercalation, which should be attributed to smaller size and weaker electrostatic interaction of H^+ comparing with that of Zn^{2+} to enable a fast diffusion kinetic in 1 × 1 tunnels of MON.[34] The combination of high reversible capacity, excellent cyclability, and rate property of MON cathode with proton and Zn-ion synergistic effects presents a potentially high-performance aqueous battery electrochemistry for practical applications, which is environmentally friendliness, safe, and low cost. The good understanding on the fundamental reactions of MON also opens a window for designing better MnO_2 cathode materials for rechargeable Zn-MnO_2 batteries using mild aqueous electrolytes.

In conclusion, a high-performance aqueous Zn/MON battery system is demonstrated based on a H^+/Zn^{2+} synergistic intercalation mechanism, as evidenced by charge/discharge profiles, XRD, XPS, ICP-MS, HR-TEM, and DFT analyses. The novel H^+ and Zn^{2+} synergistic intercalation mechanism contributes to the high reversible discharge capacity and energy density of Zn/MON cell (≈275.6 mAh g^{-1} at 0.1 C, ≈228.5 Wh kg^{-1}). The impressive cyclability of Zn/MON cell is presented, with capacity retention of 96% after 300 cycles at 0.5 C, and 79% within 2000 cycles at 6 C. Furthermore, Zn/MON cell also demonstrates an excellent rate performance of (115.1 mAh g^{-1} at 10 C), mainly due to the fast diffusion kinetics of H^+ intercalation. Thus, the presented aqueous Zn/MON cell composing zinc anode, MON cathode, and mild aqueous electrolyte holds great potential in LSES applications, attributing to its remarkable battery performance, low material cost, high safety, as well as environmental friendliness.

Experimental Section

Synthesis of Samples: The manganite nanosheet in this manuscript was prepared via a hydrothermal chemical reaction between $KMnO_4$ and acetylene black (AB). Before hydrothermal, AB was treated with concentrated nitric acid (HNO_3) at 60 °C for 12 h, and then filtered by DI water and ethanol, then followed by drying in a vacuum oven

of 80 °C overnight. The obtained AB (0.12 g) was added into 20 mL deionized (DI) water under continuous stirring (solution A). 0.79 g potassium permanganate ($KMnO_4$) was added into 15 mL DI water with string (solution B). Then, the solution B was added into solution A dropwise under string, thus, a homogeneous black suspension formed. Then, the obtained suspension was transferred to a 50 mL Teflon-lined stainless-steel autoclave, and treated hydrothermally at 120 °C for 24 h. The obtained product was filtered, washed thoroughly using water and alcohol, and dried in vacuum at 80 °C overnight. The β-MnO_2 nanorods were also synthesized through a simple hydrothermal method, as comparison. 20 mL $(NH_4)_2S_2O_8$ (0.1 M) solution was added into 20 mL $MnSO_4{\cdot}H_2O$ (0.6 M) dropwise under continuous stirring. The obtained mixture was then transferred into a 50 mL Teflon-lined stainless-steel autoclave, and maintained at 120 °C for 15 h. The obtained β-MnO_2 was centrifuged, and washed thoroughly using water and absolute ethyl alcohol, and then dried in vacuum at 80 °C overnight.

Materials Characterizations: XRD (Bruker D8 ADVANCE) using Cu Kα radiation was used to characterize the crystal structure. SEM (JEOL JSM-7100F) was used to observe the micro-morphology. AFM imaging was performed using a Bruker Multimode 8 system with a Nanoscope V controller and silicon nitride modified scanning probe. The transmission electron microscopy (TEM, Titan G2 60-300, FEI) was used to characterize the morphology and selected-area electron diffraction (SAED) patterns. XPS (ESCALAB 250) was used to explore the electronic structure and compositional information. Nitrogen adsorption tests at 77 K using a Micromeritics Tristar II 3020 instrument were applied to measure the Brunauer–Emmett–Teller (BET) surface area.

Electrochemical Test: Electrochemical performance was tested using CR2032 coin-type cells. The cathode was fabricated by blending MON, AB, and polyvinylidene fluoride (PVDF) in a weight ratio of 8:1:1 with *N*-methyl-2-pyrrolidone as solvent. The obtained slurry was pasted onto a Ti foil (≈10 µm) and vacuum-dried at 80 °C for 12 h. The loading mass of active material was ≈2.5 mg cm^{-2}. MS-PTFE membrane and zinc foil were employed as the separator and anode, respectively. A 1 M $ZnSO_4$ + 0.2 M $MnSO_4$ aqueous solution was used as electrolyte. The assembled cells were galvanostatically cycled between 1.0 and 1.8 V using the LAND-CT2001A battery-testing instrument. EIS and CV were measured on a Chi 660e electrochemical workstation (CH Instruments Ins). For EIS tests, the AC perturbation signal was ±5 mV and the frequency ranged from 100 kHz to 100 mHz. CV tests were conducted between 0.95 and 1.85 V vs Zn/Zn^{2+}, with scan rates varied from 0.1, 0.5, 1, 2, 3, and 4 mV s^{-1}.

Supporting Information

Supporting Information is available from the Wiley Online Library or from the author.

Acknowledgements

Q.Z. and X.C. contributed equally to this work. M.W. directed the DFT calculations; R.Q., J.L., W.Z., Mingqiang Liu, and K.Y. helped a lot on material characterization and elelctrochemical measurements; all authors discussed the data and commented on the manuscript; H.C. revised the English writing; F.P. directed the whole research. This work was financially supported by Soft Science Research Project of Guangdong Province (Grant No. 2017B030301013) and Shenzhen Science and Technology Research (Grant No. ZDSYS20170728102618).

Conflict of Interest

The authors declare no conflict of interest.

Keywords

aqueous Zn batteries, cycling performance, H^+/Zn^{2+} synergistic intercalation, manganite nanosheets

Received: August 13, 2019
Revised: September 10, 2019
Published online: October 7, 2019

[1] G. Fang, J. Zhou, A. Pan, S. Liang, *ACS Energy Lett.* **2018**, *3*, 2480.
[2] C. Xu, B. Li, H. Du, F. Kang, *Angew. Chem., Int. Ed.* **2012**, *124*, 957.
[3] L. Zhang, L. Chen, X. Zhou, Z. Liu, *Adv. Energy Mater.* **2015**, *5*, 1400930.
[4] L. Jiang, Y. Lu, C. Zhao, L. Liu, J. Zhang, Q. Zhang, X. Shen, J. Zhao, X. Yu, H. Li, X. Huang, L. Chen, Y. Hu, *Nat. Energy* **2019**, *4*, 495.
[5] Y. Yang, Y. Tan, G. Fang, L. Shan, J. Guo, W. Zhang, C. Wang, L. Wang, J. Zhou, S. Liang, *Energy Environ. Sci.* **2018**, *11*, 3157.
[6] C. Xia, J. Guo, P. Li, X. Zhang, H. N. Alshareef, *Angew. Chem., Int. Ed.* **2018**, *57*, 3943.
[7] J. Huang, Z. Wang, M. Hou, X. Dong, Y. Liu, Y. Wang, Y. Xia, *Nat. Commun.* **2018**, *9*, 2906.
[8] N. Zhang, F. Cheng, J. Liu, L. Wang, X. Long, X. Liu, F. Li, J. Chen, *Nat. Commun.* **2017**, *8*, 405.
[9] B. Lee, S. Y. Chong, H. R. Lee, K. Y. Chung, B. W. Cho, H. O. Si, *Sci. Rep.* **2014**, *4*, 6066.
[10] L. Boeun, R. L. Hae, K. Haesik, Y. C. Kyung, W. C. Byung, H. O. Si, *Chem. Commun.* **2015**, *51*, 9265.
[11] H. A. Muhammad, I. Saiful, Y. P. Dimas, M. Vinod, K. Sungjin, J. Jeonggeun, K. Seokhun, K. S. Yang, K. Kwangho, K. Jaekook, *Electrochim. Acta* **2018**, *276*, 1.
[12] Y. Li, S. Wang, J. R. Salvador, J. Wu, B. Liu, W. Yang, J. Yang, W. Zhang, J. Liu, J. Yang, *Chem. Mater.* **2019**, *31*, 2036.
[13] S. Zhao, B. Han, D. Zhang, Q. Huang, L. Xiao, L. Chen, D. Ivey, Y. Deng, W. Wei, *J. Mater. Chem. A* **2018**, *6*, 5733.
[14] S. Islam, M. H. Alfaruqi, V. Mathew, J. Song, S. Kim, J. Jo, J. P. Baboo, D. T. Pham, D. Y. Putro, Y.-K. Sun, J. Kim, *J. Mater. Chem. A* **2017**, *5*, 23299.
[15] C. Chen, K. Xu, X. Ji, L. Miao, J. Jiang, *ACS Appl. Mater. Interfaces* **2017**, *9*, 15176.
[16] M. H. Alfaruqi, M. Vinod, J. Gim, S. Kim, J. Song, J. P. Baboo, H. C. Sun, J. Kim, *Chem. Mater.* **2015**, *27*, 3609.
[17] S.D. Han, K. Soojeong, D. Li, V. Petkov, H. Yoo, P. J. Phillips, H. Wang, J. Kim, K. More, B. Key, R. Klie, J. Cabana, V. Stamenkovic, T. Fister, N. Markovic, A. Burrell, S. Tepavcevic, J. Vaughey, *Chem. Mater.* **2017**, *29*, 4874.
[18] S. Kohei, T. Atsumi, H. Maho, E. W. Robyn, N. Masanobu, K. Yu, O. Fumiyasu, L. O. Norihiko, K. Kiyoshi, I. Tetsu, *J. Mater. Chem. A* **2019**, *7*, 12225.
[19] N. Zhang, F. Cheng, Y. Liu, Q. Zhao, K. Lei, C. Chen, X. Liu, J. Chen, *J. Am. Chem. Soc.* **2016**, *138*, 12894.
[20] L. Wang, X. Cao, L. Xu, J. Chen, J. Zheng, *ACS Sustainable Chem. Eng.* **2018**, *6*, 16055.
[21] Y. F. Li, Z. P. Liu, *J. Am. Chem. Soc.* **2018**, *140*, 1783.
[22] A. Biswal, M. Minakshi, B. C. Tripathy, *ChemElectroChem* **2016**, *3*, 976.
[23] S. Emily, S. Jaehee, G. Karen, K. Nam, R. Gary, B. L. Sang, *Phys. Chem. Chem. Phys.* **2018**, *20*, 2517.
[24] W. Sun, F. Wang, S. Hou, C. Yang, X. Fan, Z. Ma, T. Gao, F. Han, R. Hu, M. Zhu, C. Wang, *J. Am. Chem. Soc.* **2017**, *139*, 9775.
[25] H. Pan, Y. Shao, P. Yan, Y. Cheng, K. S. Han, Z. Nie, C. Wang, J. Yang, X. Li, *Nat. Energy* **2016**, *1*, 16039.
[26] B. Lee, H. R. Seo, H. R. Lee, C. S. Yoon, J. H. Kim, K. Y. Chung, B. W. Cho, S. H. Oh, *ChemSusChem* **2016**, *9*, 2948.

[27] Y. Jin, L. Zou, L. Liu, H. E. Mark, L. P. Rajankumar, Z. Nie, K. S. Han, Y. Shao, C. Wang, J. Zhu, H. Pan, J. Liu, *Adv. Mater.* **2019**, *31*, 1900567.
[28] V. Augustyn, J. Come, M. A. Lowe, J. W. Kim, P. L. Taberna, S. H. Tolbert, H. D. Abruna, P. Simon, B. Dunn, *Nat. Mater.* **2013**, *12*, 518.
[29] D. Wang, L. Wang, G. Liang, H. Li, Z. Liu, Z. Tang, J. Liang, C. Zhi, *ACS Nano* **2019**, *13*, 10643.
[30] M. Song, H. Tan, D. Chao, H. Fan, *Adv. Funct. Mater.* **2018**, *28*, 1802564.
[31] D. Wang, H. Li, Z. Liu, Z. Tang, G. Liang, F. Mo, Q. Yang, L. Ma, C. Zhi, *Small* **2018**, *14*, 1803978.
[32] Z. Liu, F. Mo, H. Li, M. Zhu, Z. Wang, G. Liang, C. Zhi, *Small Methods* **2018**, *2*, 1800124.
[33] D. Chao, W. Zhou, C. Ye, Q. Zhang, Y. Chen, L. Gu, K. Davey, S. Z. Qiao, *Angew. Chem., Int. Ed.* **2019**, *58*, 7823.
[34] M. Liu, Q. H. Zhao, H. Liu, J. Yang, X. Chen, L. Yang, Y. Cui, W. Huang, W. Zhao, A. Song, Y. Wang, S. Ding, Y. Song, G. Qian, H. Chen, F. Pan, *Nano Energy* **2019**, *64*, 103942.

